Simultaneous optical coherence tomography and Scheimpflug imaging using the same incident light

Xiaoran Li,[1] Samuel Lawman,[1,2] Bryan M. Williams,[2] Sicong Ye,[1] Yaochun Shen,[1,*] ⓘD and Yalin Zheng[2] ⓘD

[1]*Department of Electrical Engineering and Electronics, University of Liverpool, Liverpool L69 3GJ, UK*
[2]*Department of Eye and Vision Science, University of Liverpool, Liverpool L7 8TX, UK*
*y.c.shen@liverpool.ac.uk

Abstract: For any single anterior chamber cross-sectional (tomographic) imaging method, there is a practical compromise between image size and image resolution. In order to obtain large field-of-view cross-sectional images of the whole anterior chamber and high-resolution cross-sectional images of the fine corneal layers, measurements by multiple devices are currently required. This paper presents a novel raster scanning tomographic imaging device that acquires simultaneous large field-of-view Scheimpflug (12.5 *mm* image depth, 50 *μm* axial resolution in air) and high-resolution spectral domain optical coherence tomography (SD-OCT) (2 *mm* image depth, $3.7 \mu m$ axial resolution in air) using the same illuminating photons. For the novel raster scanning 3D Scheimpflug imaging, a tunable lens system together with numerical methods for correcting refraction distortion were used. To demonstrate the capability of simultaneous measurement of both fine corneal layers and whole anterior chambers topology, *ex vivo* measurements on 12 porcine and 12 bovine eyes were carried out. There is a reasonable agreement in the overall central corneal thicknesses (CCT) obtained from the simultaneous SD-OCT and Scheimpflug measurements. In addition, because the same infrared light beam was used to illuminate the sample, both OCT and Scheimpflug images were taken at the exact same location of a sample simultaneously in a single measurement. This provides a unique method for measuring both the thickness and the refractive index of a sample.

1. Introduction

Cross-sectional imaging of the anterior segment is important in clinical studies and practice as it resolves the depth locations of pathologies. The anterior segment, which is responsible for the correct optical formation of images on the retina, comprises both relatively large structures such as the cornea, lens, iris, and anterior chamber and smaller structures within the cornea itself. The cornea is the outermost part of the anterior segment and contributes most of the eye's focusing power. It is composed of relatively thin layers, including the corneal epithelium, Bowman's layer, Descemet's membrane and corneal endothelium. The thickest layer in the cornea is the stroma, which is composed of multiple thin layers of lamella and individual kerotocyte cells [1]. There are many medical conditions that have optically observable effects on both small and large scale structures in the anterior segment, such as corneal scarring [2], glaucoma [3], keratoconus [4], Fuchs dystrophy [5], uveitis [6], multiple types of infectious keratitis and corneal ulcers [7].

The first devices used by clinicians to visualise the cross-section of anterior segment structures were slit lamp microscopes [8]. A slit of light is shined into the patient's eye to illuminate a cross-section of the anterior segment. This illuminated cross-section is then observed or imaged at an angle to the illumination, with a device such as a bio-microscope. A refinement of this

method is to modify the imaging optics to the Scheimpflug principle, which has been known since at least the start of the 20th century [9]. In contrary to a standard imaging device where the lens plane, detector plane and plane of focus (PoF) are parallel, a Scheimpflug imaging (SI) device modifies the alignment of the optical system so that clear images can still be obtained even when the lens plane is not parallel to the detector plane. This is achieved by ensuring that the configuration of the detector plane, lens plane and the PoF meets the Scheimpflug principle [10,11]. Fixed Scheimpflug cameras for anterior segment imaging were emerging clinically by 1990 [12,13]. An extension to this method is to rotate the device during image acquisition, allowing a full volumetric three-dimensional (3D) image of the anterior segment to be acquired. The first such commercial device, named Zeiss SLC (Carl Zeiss Meditec, Jena, Germany), was reported in 2006 [14]. 3D data from these devices are now routinely utilised for Pachymetry (measurement of corneal thickness), corneal topography, anterior and posterior corneal curvature and astigmatism determination [15,16]. For the imaging of the whole anterior segment, clinical Scheimpflug imaging systems offer a large image depth and field-of-view at the expense of relatively low image axial resolution (about 50 μm). Such a resolution is not sufficient to resolve the thin layers of the cornea.

Optical coherence tomography (OCT) is a cross-sectional imaging technique that uses low-coherence light to capture micrometre-resolution images [17]. As it is based on low coherence interferometry, its axial resolution is ultimately determined by the spectral bandwidth of the illumination light and thus is decoupled from the system's optics. As a result, an OCT system can be designed with a large depth of field illumination, which can be utilised for large field-of-view Scheimpflug imaging, but OCT itself retaining a high axial resolution. OCT was first demonstrated for imaging the cornea and anterior segment in 1994 [18], and has since been widely applied clinically [19]. For imaging the fine structures of the cornea, OCT systems can be built with ultra-high axial resolution (< 3 μm in air), with demonstrated diagnostic potential and benefits [20,21]. However, for frequency-domain OCT devices, high axial resolution requires wide spectral range whilst large image depth requires high spectral resolution. There are practical constraints to have an OCT spectrometer to have both wide spectral range and high spectral resolution whilst maintaining reasonable speed required for in vivo imaging applications. Like all imaging techniques, there are some practical compromises between image resolution, image size and image speed. Consequently, a conventional OCT system with sufficiently high axial resolution to resolve the thinner layers of the cornea, does not have the image field-of-view (axial and lateral) to capture the whole anterior chamber in a single image in a timely manner.

Both OCT and SI devices are now well-established for anterior segment imaging in clinical settings. The useful field-of-view of OCT image is limited not only by the lateral scanning areas but also by its image depth because of the curvature of corneal surface (anterior corneal radius of about 8mm). An OCT system can be engineered to image the cornea with a high axial resolution, enabling it to resolve the thin corneal layers, though the entire anterior segment will not be covered in a single measurement. Diversely, an OCT system can also be engineered to have very large image depth but its axial resolution will be limited (for example, Zeiss Visante OCT has 6 mm image depth and 18 μm axial resolution) [22]. In this study, the OCT system is engineered to provide high resolution detail and not large image depth. In addition, a typical SI system can image the anterior segment but its axial resolution is insufficient to resolve all fine layers of the cornea. As a result, in order to obtain both high-resolution images of the cornea and large field-of-view image of anterior segment, a patient may need to have two separate examinations, e.g., to be imaged by using both a high axial-resolution OCT device, and a low axial-resolution Scheimpflug device or a dedicated anterior segment OCT device. Alternatively, multiple measurements with different eye orientations and image mosaicing in post-processing can be applied to achieve a large FOV. However, there may exist image alignment problem and motion artefacts associated with the relatively long acquisition time (<1 minute). Therefore, there

is a need for a novel imaging system that can carry out high-resolution and large field-of-view imaging simultaneously.

The nature of the arrangement of the two devices provides an opportunity to add a SI system to a conventional OCT system without compromising its performance. The OCT system is built to collect the directly back scattered light while SI captures the 'side' scattered light, so the two detection systems do not impinge on each other's physical space. In this paper, we describe such a novel device combining a scanning point spectral domain (SD)-OCT and a Scheimpflug system, which can obtain OCT images with high axial resolution for examining fine corneal layers and Scheimpflug images with large field-of-view image for visualization of the anterior segment of the eye. To the best of our knowledge, this is the first time that OCT and Scheimpflug images have been simultaneously captured using the same illuminating photons. In addition, because the same infrared light beam was used to illuminate the sample, both OCT and Scheimpflug images were taken simultaneously at the exact same location of a sample in a single measurement. This provides a reliable measurement method that could be used either for cross validation of the thickness measurement using OCT and SI, or for measuring both the thickness and the refractive index of a sample.

2. Methods and materials

2.1. New device combining SD-OCT and SI system

Figure 1 show a schematic diagram of the novel imaging device combining SD-OCT and SI systems that share a single light source. The SD-OCT is based on a Michelson low-coherence interferometer setup, consisting of a wideband 2×2 single mode fiber coupler (TW850R5A2, Thorlabs, UK). The light source is a broadband superluminescent light emitting diodes (SLED) with a center wavelength of 840 *nm* and a full width at half maximum bandwidth of 130 *nm*. The output of the light source is connected to the input port of the fiber coupler which splits the input light into reference arm and sample arm. Two identical fiber collimators (F220SMA-850, Thorlabs, UK) are used in sample and reference arms, providing collimated beams of 2.4 *mm* in diameter. The collimated beam of the sample arm, after passing through a 2D Galvo Scanner (Thorlabs, GVS002), is focused onto a sample using an achromatic doublet lens (f=50 *mm)*. The light spot size at the focal point is estimated to be 22 *μm* and the light power at the sample position is measured to be 1.8 *mW*. An identical achromatic doublet is used in the reference arm in order to minimize the dispersion mismatch between the sample and the reference arms. The light returning from both reference and sample arms is recombined at the fiber coupler and sent to the spectrometer for detection . A commercial spectrometer (Wasatch Photonics, Cobra-S 800) was used, which has a spectral resolution of 0.09 *nm*, providing an imaging depth of 2.0 *mm*. The maximum data acquisition rate of the spectrometer is over 100,000 A-scans/s although in all experiments reported here the A-scan rate used was 10,000 A-scans/s. Each B-scan contains 1000 A-scans thus the acquisition time for each B-scan was 0.1s. The signal to noise ratio (SNR) was measured to be over 75 dB.

For SI, the principal plane of the imaging lens, the illumination plane and the image plane are arranged according to the Scheimpflug principle, i.e. the plane of imaging lens and the image plane extended meet at a line through which the plane of illumination also passes, as shown in Fig. 1. The imaging lens comprises an electrically tunable lens, which is synchronized with the beam steering of the Galvo-scanner, allowing the Scheimpflug configuration requirement to always be approximately met during 3D scans. Two identical SI systems that work independently are placed on opposite sides of the illumination plane so that good quality images can always be obtained for both sides of the eyeball. A pair of polarizers were used to minimize the light reflected from the cornea surface from entering into the SI device during 3D scans. The acquisition speed is 0.1s per B-scan, and the achieved SNR is about 16 dB. Note that both OCT
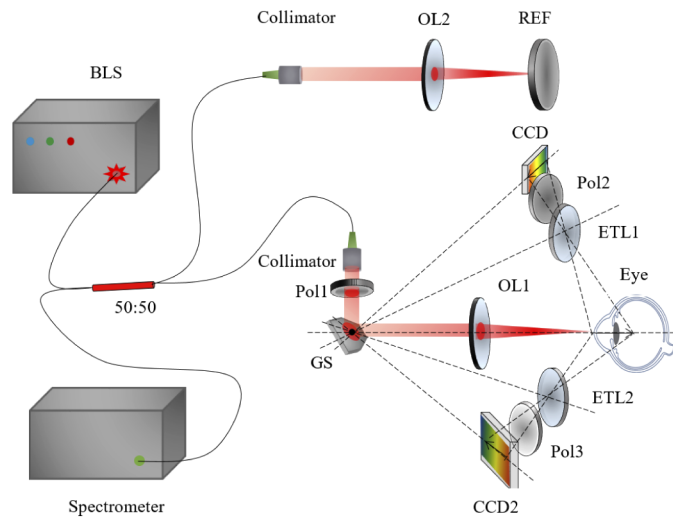
Fig. 1. Schematic diagram of our new imaging device. BLS: Broadband light source; OL1, OL2: Objective lens; REF: Reference mirror; OLS1, OLS2: Optical lens system; GS: Galvo scanner. Electrically tunable lens; Pol1-3: Polarizer.

and SI use the same illuminating light, therefore they both measure simultaneously at the same location of the sample.

2.2. Sample preparation and image segmentation

To demonstrate the performance of the imaging device, fresh porcine (C.S. Morphets and Sons Ltd, Widnes, UK) and bovine (G & Gb Hewitt Ltd, UK) eyes were obtained from a local abattoirs. Enucleation was carried out before carcass processing with boiling water to maintain cornea transparency and structure. The measurements were taken within 24 hours of post-mortem. The eyeballs were held using a custom 3D printed hollow plastic holder during the measurements. In total, 12 bovine eyes and 12 porcine eyes were measured.

In order to quantify the thickness of the corneal layers, we use a gradient based segmentation method to extract the corneal interfaces for OCT and Scheimpflug images [23]. The proposed method comprises two procedures: the first step is to roughly estimate the interface region of the cornea and the second step is to determine the interface position accurately.

The front surface (air-epithelium interface) of the cornea is the first interface to be extracted. The main feature used to search the interface region is the bright-to-dark or dark-to-bright transitions along depth direction. The interface region can be estimated to be the highest intensity based on a prior assumption of the signal intensity. Then, a customised method is used to refine the interface estimated above, by finding the maximum absolute vertical gradient. Since the SNR at the central cornea is relatively higher than peripheral region, the interface positions can be readily found at the central cornea. In order to improve the segmentation robustness at the peripheral region, the segmentation starts from the central region to the peripheral region where the corneal back surface may not always visible clearly..

Once the front surface of the cornea is determined, other layers can be firstly estimated using the predetermined front surface as their curve profiles are similar. Other layer interfaces can be finally determined by maximizing the summation of absolute gradient in the region below the front surface.

2.3. Correction method for corneal thickness measurement

The precise measurement of cornea thickness is important to the diagnosis and the follow-up of eye diseases and the refractive surgery. For example, the cornea thickness increases in the patients with cornea guttata received the dorzolamide therapy, and consequently needs monitoring [24,25]. It may also assist in discriminating eye diseases, such as keratoconus [26,27] and glaucoma [28].

In OCT measurement, OCT image provides the optical path length (with the assumption of the EM radiation traveling at the speed of light in a vacuum) of the cornea (T_o), the physical cornea thickness (AE in Fig. 2) can be calculated as the ratio of the measured optical path length over its group refractive index n_G:

$$AE = \frac{T_O}{n_G}. \tag{1}$$

In SI measurement, one has to consider the effect of the optical refraction in order to calculate the actual cornea thickness [29]. As shown in Fig. 2, the cornea thickness (AD) appeared in the Scheimpflug image will be smaller than the actual thickness of the cornea (AE). This can be corrected according to Snell's law as followings [29]:
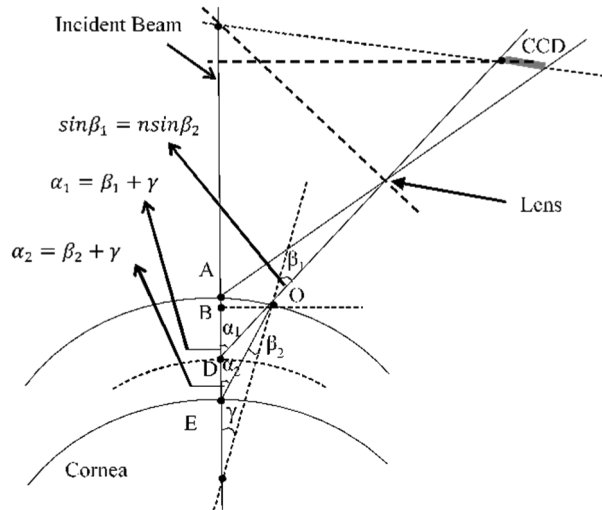

Fig. 2. The optical paths of the SI system, where AE is the actual thickness of the medium, AD is the thickness captured by the camera and n is the refractive index of the cornea.

As shown in Fig. 2, assuming incident beam is orthogonal to the corneal apex, angle α_1 can be first calculated by

$$\tan \alpha_1 = \frac{FC}{FA + AD}. \tag{2}$$

Assuming the known radius of eye (R), the angle γ and BO can be obtained by solving following equations:

$$\left(\frac{BO}{\tan \alpha_1} + R - AD \right)^2 + BO^2 = R^2, \tag{3}$$

$$\sin \gamma = \frac{BO}{R}. \tag{4}$$

Finally the physical corneal thickness AE can be calculated:

$$AE = \frac{BO}{\tan \alpha_2} - \frac{BO}{\tan \alpha_1} + AD. \tag{5}$$

In the above equations, we assumed a known refractive index in order to calculate the cornea thickness. As mentioned above, both OCT and SI measures the sample simultaneously at the exact same location because a single light illumination was used, the physical corneal thickness measured by two devices should be same:

$$AE = \frac{BO}{\tan(\arcsin\frac{\sin\beta_1}{n} + \gamma)} - \frac{BO}{\tan\alpha_1} + AD. \tag{6}$$

This provides an excellent technique to calculate simultaneously both the layer thickness and the refractive index of cornea by solving Eqs. (1) and (6).

2.4. Correction for the refraction distortion of Scheimpflug image

During 3D scanning, when the light beam scans across the sample in the direction that is perpendicular to the illumination plane, its image on the CMOS camera will change as well (Fig. 3(a)). Consequently, the surface of a sample will appear to be "tilted" in the obtained SI images, as shown in Fig. 3(b). In order to correct this, we will describe how to calculate the image position "D" as a function of the scan angle β (Fig. 3(c)) as follows:
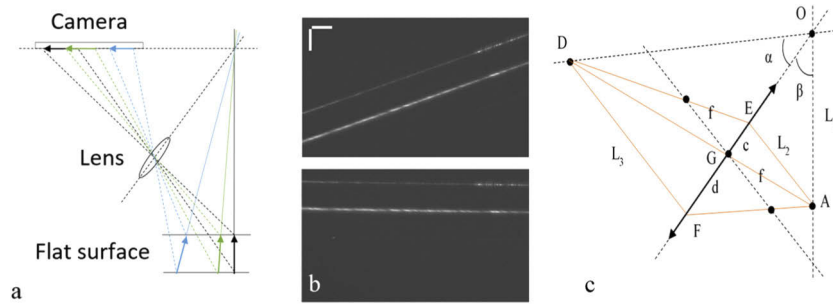

Fig. 3. (a) A diagram showing the change of the image position when the optical beam scans across the sample in the direction that is perpendicular to the illumination planes. (b) The reconstructed Scheimpflug image of a microscope slide before (top) and after (bottom) distortion correction. Scale bar is 1 *mm*. (c) A diagram showing geometrical relationship of the top of the object (A) and its imaging position (D)

In the following calculations, we assume OA is the length between the intersection point (O) and the object A; f is the focal length of the imaging lens; α is the angle between camera plane and lens plane and β is the angle between illumination beam and lens. During 3D scanning, the angle β will change. We would like to calculate the change of the position D as a function of β. From Fig. 3(c), we have:

$$\frac{f}{EA} = \frac{FG}{EG + FG} \tag{7}$$

$$\frac{EA}{DF} = \frac{EG}{FG}. \tag{8}$$

From Eqs. (7) and (8), Eq. (9) can be obtained:

$$DF = \frac{f \times EA}{EA - f}. \tag{9}$$

And EA can be expressed by OA:

$$EA = OA \times \sin\beta. \tag{10}$$

From Eqs. (3) and (4), the length of OD can be expressed as:

$$OD = \frac{DF}{\sin \alpha} = \frac{f \times OA \times \sin \beta}{(OA \times \sin \beta - f) \times \sin \alpha}. \tag{11}$$

In order to validate this distortion correction method, we measured a microscope slide which was placed perpendicular to the incident beam. Figure 3(b) shows the resultant SI image before and after distortion correction. After the distortion correction, an expected flat surface is obtained, validating the proposed distortion correction method. Note that OCT measurement was used to check and confirm that the microscope slide was indeed placed normally to the light beam.

3. Results and discussion

3.1. System performance

To quantify the axial resolution of the OCT system, a glass plate with flat surface was measured. Figure 4 shows the resultant experimental raw axial Point Spread Function (PSF) (black line) of the glass interface, together with the theoretical PSF (blue line) which is defined as the Fourier transform (FFT) of the reference spectrum. In order to compare the two PSFs, the axial axis is shifted so that they are at the same location, and amplitudes are normalised. The theoretical and experimental PSFs closely match. Axial resolution, as determined by the full width at half maximum (FWHM) of the main peak is 3.7 μm in air, which corresponds to 2.7 μm in corneal tissue (n_G=1.376). In addition, the imaging depth of the OCT system achieved was 1.98 mm (in air), determined by the spectral resolution of the spectrometer used.
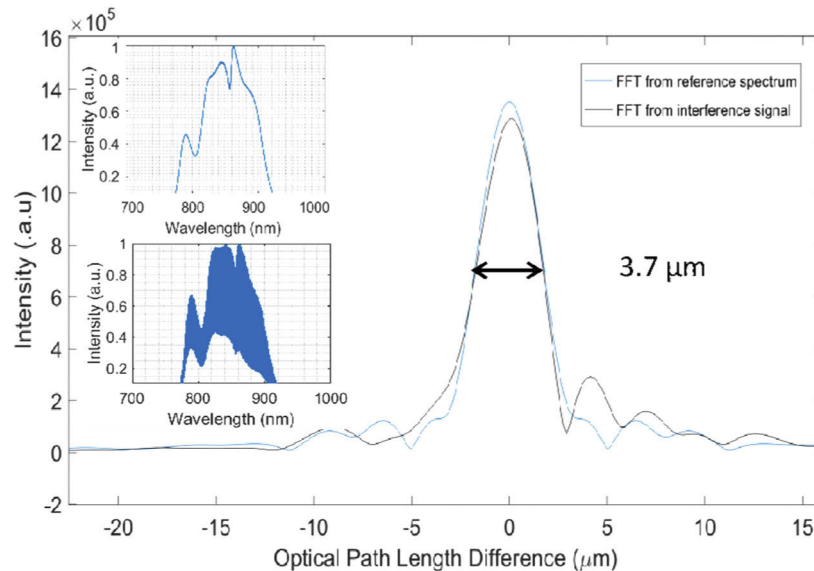

Fig. 4. A-scan (the depth profile) of a piece of glass measured via OCT. Blue and black line indicates FFT signals of reference and interference spectra, respectively. (Inset) example raw reference and interference spectra in wavelength space.

To quantify the axial resolution of the SI system, the same glass plate was measured. Figure 5(a) shows the SI image of the microscope slide together with the depth profile at the centre position of the microscope slide. The full width at half maximum (FDHM) of the first and second peak of the depth profile was determined to 52 μm and 50 μm, respectively, indicating that an axial resolution of 50 μm was achieved. In addition, the peak position distance between the first and

second peak was determined to be 490 *μm*. By correcting the diffraction effect (section 2.3) using the geometric dimensions of the SI configuration, the physical thickness of the microscope slide can be calculated to be 0.98 mm which agrees with the thickness (1.01 *mm*) measured using a digital caliper . In addition, OCT image taken on the glass slide also revealed the front and back surface of the glass slide separated by an optical pathlength of 1.48 mm, corresponds a physical thickness of 0.98 *mm* at a refractive index of 1.51 [30].
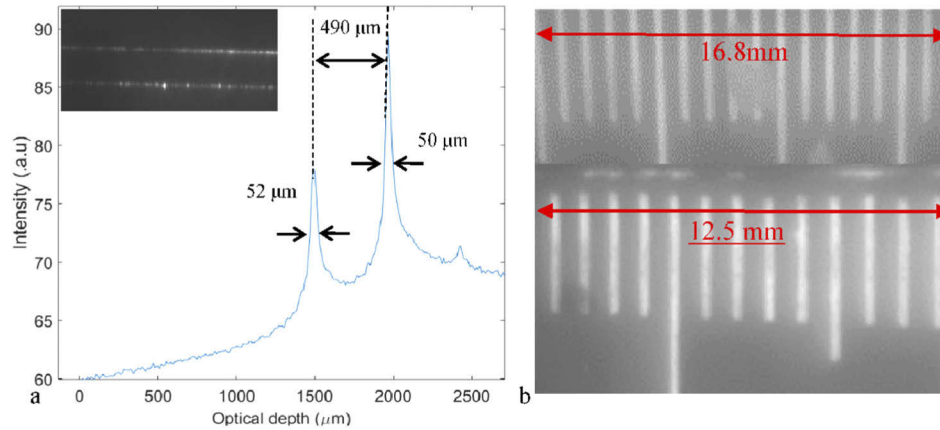

Fig. 5. (a) SI image of a microscope slide and an averaged depth profile. (b) SI images of a ruler showing the lateral (top) and axial (bottom) imaging range.

In order to quantify the imaging field-of-view, a ruler is placed in the plane of the OCT probe beam. In this experiment, the ruler was illuminated by a separate light source and Fig. 5(b) shows the image obtained using the SI imaging optics. As shown in Fig. 5(b), (a) maximum imaging range of 16.8 *mm* and 12.5 *mm* have been achieved in the lateral and axial/depth directions, respectively. This provides the capacity of covering the anterior segment.

Table 1 summarizes the main performance of two devices. It is clear that OCT has higher axial resolution whilst SI provides wider imaging range (field-of-view). Note that considering the refraction distortion of Scheimpflug image when imaging eyes and the actual imaged depth will be larger than 12.5 *mm*, as discussed in Fig. 2 in section 2.3.

Table 1. Comparison of the OCT and SI in imaging depth and axial resolution.

	Imaging depth in air (*mm*)	Lateral imaging range (*mm*)	Axial resolution (*μm*)
OCT imaging	1.98	5–6[a]	3.7 (in air)
Scheimpflug imaging	12.5	16.8	50

[a]Effectively restricted by the curvature of corneal samples in this study.

3.2. Imaging the porcine and bovine eyes

Figure 6 shows a Scheimpflug image of the anterior segment of a porcine eye and an OCT B-scan of the centre portion of the porcine cornea obtained simultaneously using the combined SI and OCT device. Only the central portion of the cornea can be effectively imaged by OCT because of its limited image depth and the surface curvature of the cornea. Nevertheless, the epithelium, stroma and endothelium can be clearly resolved in the OCT image. The SI, however, could not resolve individual corneal layers of the porcine eyes. On the other hand, the Scheimpflug image displays the anterior segment of the eye including cornea (both front and the back), lens (the front), and iris, for which the OCT system did not have the imaging range. At the bottom

of the image is the iris, which scatters the NIR light much more strongly than the other parts of the anterior segment, resulting in the saturation of the camera sensor. The ciliary body is obscured/merged in the iris because of the limited signal to noise ratio (SNR) and dynamic range of the SI image.
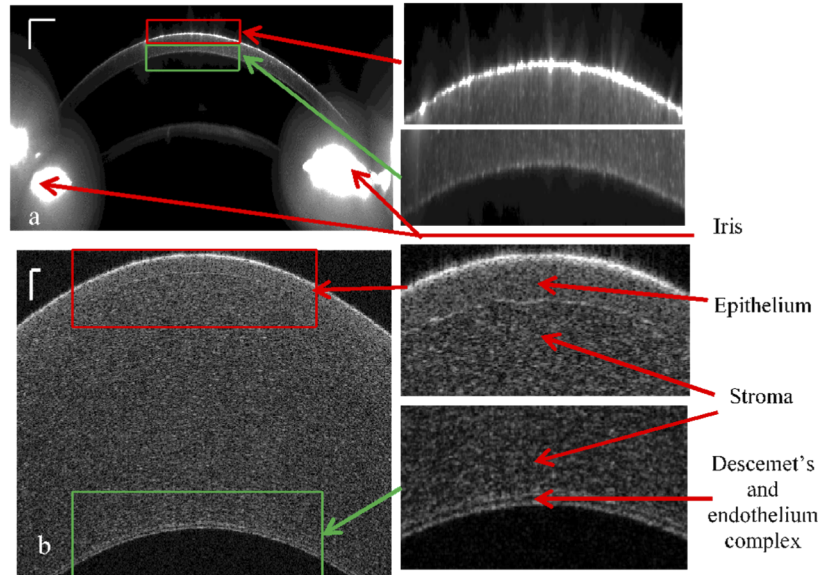

Fig. 6. Example images of a porcine cornea. (a) Scheimpflug image of the anterior segment structure of a porcine eye. The scale bar is 1 *mm.* (b) OCT image of fresh porcine cornea. The corneal epithelium and endothelium are enlarged shown on the right. The scale bar is 100 *μm.*

Figure 7 shows a Scheimpflug image of the anterior segment of the bovine eye and an OCT B-scan of the center portion of the bovine cornea. Again, the epithelium, the combined Descemet's and Endothelium complex can all be resolved clearly in OCT images (Fig. 7(b)). Diversely, the Scheimpflug image can visualize the anterior segment of the bovine eye. Because the epithelium of bovine cornea is in general thicker than that of the porcine cornea, Scheimpflug can resolve the bovine corneal epithelium, although not as clearly as OCT. Note that not all bovine cornea epithelium layer can be resolved because of the thickness variation amongst cornea samples, as will be shown in the next section.

3.3. Quantification of central corneal thickness

In order to study the correlation between corneal thicknesses measured using OCT and SI, 12 porcine and 12 bovine eyes were measured. Figure 8 shows OCT and SI images of central cornea for 12 porcine and 12 bovine eyes. The aforementioned image segmentation is subsequently used to find corneal layer interfaces and the identified layer interfaces are highlighted in Fig. 8. The corneal thickness at the corneal central positions can then be obtained from these segmented SI and OCT images. Table 2 summarizes the resultant "raw" overall corneal thicknesses. Note that these corneal thickness obtained from OCT and SI images are "raw" values and have not been corrected. According to Eqs. (1) and (6), in order to get the real physical thickness of cornea, the OCT corneal thickness (optical path length) will have to be divided by group refractive index whilst the effect of the refraction on the SI corneal thickness will also have to be corrected.

Since both OCT and SI measurements took place simultaneously at the exact same cornea position illuminated by the same light beam, the physical thickness of the cornea obtained by
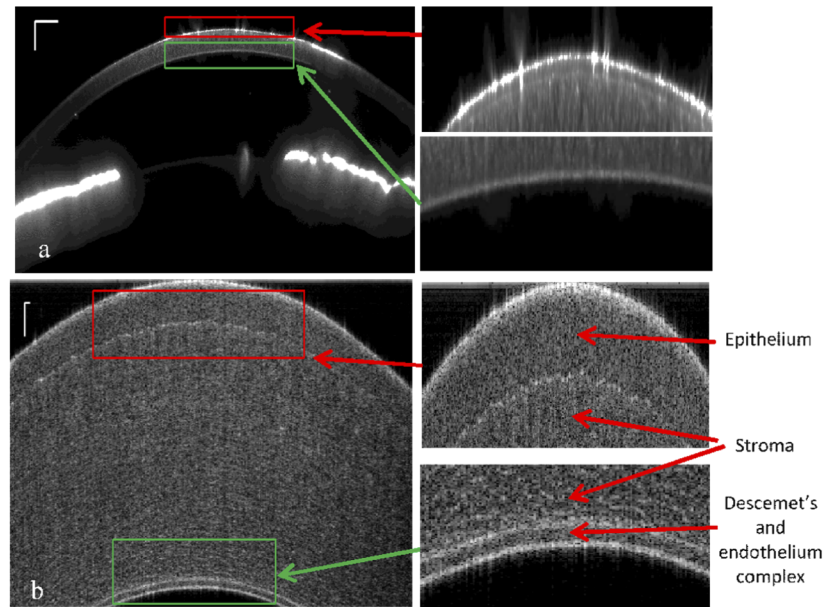
Fig. 7. (a) Scheimpflug image of the anterior segment structure of the bovine eye. The scale bar is 1 *mm*. (b) OCT image of fresh bovine cornea. The corneal epithelium and endothelium are enlarged shown on the right. The scale bar is 100 *μm*.

Table 2. The measured raw OCT and SI thicknesses and the calculated refractive index.

Samples	Porcine				Bovine			
	T_0	AD	AE	RI (n)	T_0	AD	AE	RI (n)
1	1057	536	779	1.357	1225	583	891	1.375
2	1151	572	846	1.361	1293	601	938	1.379
3	1138	562	834	1.364	1403	652	1009	1.390
4	1145	550	829	1.381	1373	635	986	1.392
5	1298	626	938	1.384	1298	659	959	1.353
6	1152	582	853	1.351	1659	768	1188	1.396
7	1206	623	887	1.359	1251	587	906	1.381
8	1346	648	971	1.386	1372	667	1007	1.362
9	1200	586	871	1.373	1500	665	1056	1.420
10	1194	635	891	1.340	1526	680	1076	1.418
11	1172	543	834	1.405	1435	655	1025	1.401
12	1193	601	881	1.354	1511	680	1072	1.410
RI from regression analysis				1.373				1.397

OCT and SI should be the same (assuming measurement plane is across the apex). This provides a method for measuring the RI of each individual cornea sample. Using Eqs. (1) and (6), the RI values of each individual cornea sample can be calculated, as shown in Table 2. Then, the averaged RI can be calculated as the slope of linear regression analysis between corrected SI corneal thickness and the original OCT corneal thickness (slope of is named as averaged RI). The averaged RI for these groups of porcine and bovine corneas are determined to be 1.373 ± 0.018
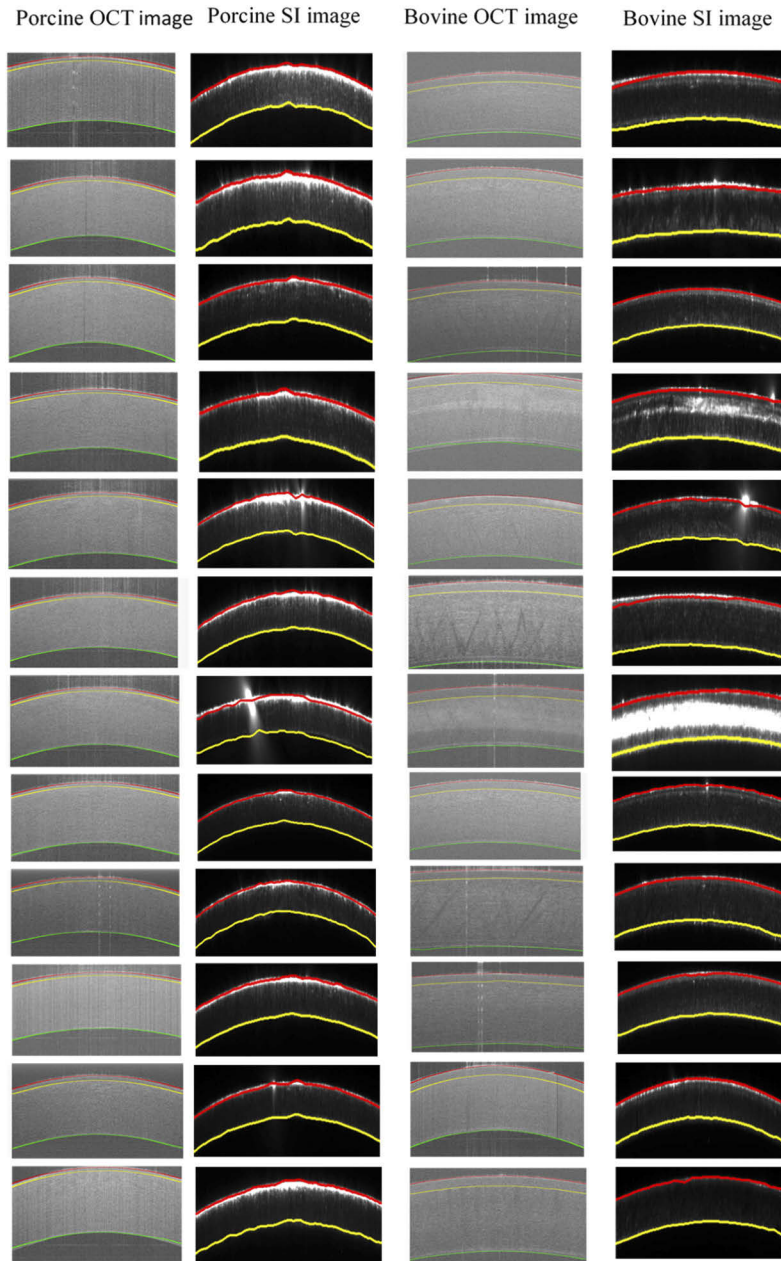
Fig. 8. The OCT and SI images of 12 porcine and 12 bovine eyes with marked layers interfaces

and 1.397 ± 0.021, respectively. They are within the range of previously reported values [1]. Note that for simplicity we used the averaged RI here as a hybrid approximation. In reality, there is a slight difference between the phase and the group refractive index of cornea [31,32].

In addition, it should be pointed out that SI measures the intensity of the light scattered/reflected back from the eye whilst OCT measures the electric field of the light scattered/reflected back from the eye. As evident from Fig. 8, OCT method provides larger dynamic range than SI imaging method. For example, the SI images of the 4th and 7th bovine eye show signs of saturation whilst their corresponding OCT images are not. This is expected as the electric field, which OCT measures, is proportional to the square root of the light intensity which SI measures. Therefore OCT usually has better image quality and SNR, able to resolve all epithelium layers in both porcine and bovine eyes whilst SI cannot resolve epithelium layer in porcine eye. In addition, the intensity saturation of some SI images particularly at the front surface of cornea was an issue for precisely calculation of the corneal thickness. To partially mitigate this, we calculated the mean corneal thicknesses over 100 pixels near the corneal apex (the range covers 1.1 *mm*, approximately).
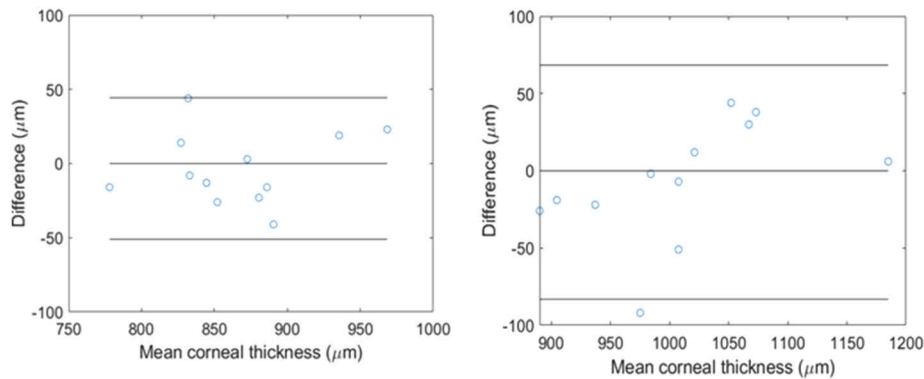

Fig. 9. The Bland-Altman-plot to display the agreement between OCT and SI measurements for porcine (left) and bovine (right) eyes. The middle horizontal line is the average difference whilst the top and bottom horizontal lines are +/- 1.96 standard deviation.

The measurement of corneal thickness is important for many clinical applications. In the following we will use the averaged refractive index value to calculate the corneal thicknesses of each individual eye. Table 3 summarizes the layer thicknesses of 12 porcine eyes and 12 bovine eyes, obtained using OCT and SI. OCT provides high axial resolution, which enables the thickness of both the epithelium layer and the overall corneal thickness to be determined, whilst SI can only provide the overall corneal thickness because of its limited SNR and axial resolution. All measured thicknesses of the porcine corneas are within the range of previously reported values [1,33–35].

In order to determine the correlation between corneal thicknesses measured by both techniques, Pearson's correlation is used to measure the strength of the association. The R values (value of Pearson's correlation coefficient) of the porcine and bovine groups are 0.90 and 0.92, respectively. It shows the thicknesses measured by OCT and SI perform high positive correlation (For R, it indicates no linear correlation when it closes to 0, it indicates positive linear correlation when it closes to 1). As a further illustration, Fig. 9 shows Bland-Altman-plot to display the agreement between OCT and SI measurements for porcine and bovine eyes. The X-axis represents the averaged overall corneal thickness of OCT and SI measurements and Y-axis shows the difference between OCT and SI measurements. In Fig. 9, upper and lower lines are determined by the standard deviation (s) of the differences between OCT and SI measurements. It indicates that

Table 3. The thickness of epithelium layer measured by OCT and corneal thickness measured by OCT and Scheimpflug. The average and the standard deviation were calculated from 100 points measurement values at the central region.

	Epithelium (μm)	Overall corneal thickness (OCT, μm)	Overall Corneal thickness (SI, μm)
Porcine 1	55 + 1.0	770 + 1.6	786 + 9.7
Porcine 2	48 + 0.7	838 + 0.8	851 + 7.2
Porcine 3	55 + 1.0	829 + 2.3	837 + 4.1
Porcine 4	52 + 0.9	834 + 1.0	820 + 4.9
Porcine 5	52 + 0.8	945 + 0.9	926 + 11.8
Porcine 6	49 + 1.0	839 + 1.5	865 + 10.8
Porcine 7	46 + 1.0	878 + 2.1	894 + 6.2
Porcine 8	58 + 0.8	980 + 1.2	957 + 6.0
Porcine 9	57 + 0.7	874 + 1.2	871 + 7.7
Porcine 10	52 + 1.4	870 + 0.9	911 + 9.0
Porcine 11	71 + 0.7	854 + 1.0	810 + 5.0
Porcine 12	47 + 1.0	869 + 0.9	892 + 8.3
Bovine 1	128 + 0.9	877 + 0.9	903 + 7.9
Bovine 2	123 + 0.9	926 + 0.9	948 + 12.6
Bovine 3	122 + 1.0	1004 + 1.4	1011 + 9.4
Bovine 4	142 + 2.1	983 + 3.2	985 + 9.4
Bovine 5	136 + 1.1	929 + 1.5	1021 + 11.0
Bovine 6	147 + 0.8	1188 + 2.2	1182 + 9.4
Bovine 7	173 + 1.4	895 + 1.3	914 + 7.8
Bovine 8	134 + 0.8	982 + 0.7	1033 + 4.7
Bovine 9	122 + 1.3	1074 + 1.4	1030 + 4.7
Bovine 10	128 + 1.7	1092 + 1.6	1054 + 15.7
Bovine 11	152 + 0.6	1027 + 1.0	1015 + 9.4
Bovine 12	143 + 1.0	1082 + 0.9	1052 + 7.9

except for one bovine sample, others are all lie within ±2s of the mean difference, which shows good agreement between OCT and SI on corneal thickness quantification.

However, there are still some discrepancies between the measured OCT and SI corneal thicknesses, and 1–2 outliers in particular show large discrepancy (they were also included in the regression analysis). Firstly, these discrepancies were only observed when we assume a single refractive index for all porcine (n=1.373) and bovine (n=1.397) eyes, whilst in practice different porcine eyes may have different refractive index values. Note that OCT and SI will always give identical corneal thickness if different refractive index values were used, as shown in Table 2 where AE always equals To/n. Secondly, the discrepancy could also be caused by the intensity saturation of SI images at some positions particularly at the front and back corneal surfaces, which in turn will affect the accuracy of image segmentation (Fig. 8). In addition, the discrepancy might also be caused by the SI thickness correction method in that: (1) The thickness correction method for Scheimpflug requires a known radius of the eye. For simplicity, in our calculation we assumed a spherical shape with a fixed radius of 8 *mm* and 15 *mm* for porcine and bovine eyes, respectively. In reality, each porcine and bovine eye may have a slightly different radius and shape. As shown in Table 4, the radius will affect the calculated corneal thickness. A 2-mm-change of the radius will lead to about 10–15 *μm* change in the calculated corneal thickness. (2) In addition,

the thickness correction method for Scheimpflug is correct only if the cross-sectional image is taken at the centre position of the cornea. This may not be guaranteed during the SI measurement and any deviation from the central cornea may lead to additional discrepancy of the measured thickness. This issue could be addressed if 3D scans could be carried out on the eyes that would allow both the centre and curvature radius of the cornea to be experimentally determined.

Table 4. Comparison of corneal thickness with different radius for porcine corneas.

	Cornea (SI before correction, μm)	Cornea (SI after correction, R=7, μm)	Cornea (SI after correction, R=8, μm)	Cornea (SI after correction, R=9, μm)
Porcine 1	526	780	786	791
Porcine 2	572	844	851	856
Porcine 3	562	831	837	842
Porcine 4	550	814	820	825
Porcine 5	626	919	926	932
Porcine 6	582	858	865	870
Porcine 7	623	887	894	900
Porcine 8	648	949	957	963
Porcine 9	586	864	871	876
Porcine 10	635	904	911	917
Porcine 11	543	804	810	815
Porcine 12	601	885	892	897

3.4. 3D OCT and SI measurements

The standard method currently used by commercial SI systems to perform 3D scanning is to rotate the illumination optics and camera together in a circle around the object plane centred at the pupil. This results in the capture of radial Scheimpflug cross sectional images at the different rotation angles. During the rotation procedure, the imaging plane is always located at the focal point of the imaging system. In order to avoid the complex electro-mechanics to rotate the whole system, we instead used a Galvo scanner to steer a scanning point light beam which is standard in clinical OCT systems. The resulting issue of this is that in the combined SI and OCT device, the camera and lens are in fixed positions, while the illuminating plane is moving. Therefore, during 3D imaging the light illumination planes may fall outside the depth of focus of the SI optics, thus ruining image clarity, over much of the imaged volume. To overcome this, two (one for each SI system) electrically tunable lenses were utilized to allow clear images of the illumination plane of the SI/OCT device to be formed at the SI imaging plane, without the need to mechanically move the CMOS camera.

In addition, during 3D scanning the light beam is steered across the eye and at specific angles the light specularly reflected from the surface of the eye, rather than the desired diffusely scattered light, may dominate the received signals. In order to minimize this reflection artefact, a polariser (LPNIRE100, Thorlabs, UK) was placed on the incident beam path and another polariser was placed before the CMOS camera.

In order to demonstrate the 3D imaging capability of the device, two porcine eyes were imaged by OCT and SI, respectively. The current OCT setup offers a data volume of 1024 (depth) × 1000 (lateral) × 420 (horizontal), covering a scanning area of 15.2 *mm* (lateral) × 8.8 *mm* (horizontal). The OCT image depth is 2 *mm* (depth). The SI setup offers a data volume with the size of 1200 × 1920 × 420 that covers the same scanning area as the OCT measurement. The SI imaging depth is 12.5 *mm* (Table 1). The required acquisition time for a full 3D OCT and SI scans are 42s, mainly limited by the data transfer from the CMOS camera and the spectrometer to the computer.

However, with data acquisition rate of 10,000 A-scan per second, there is room for improvement in image acquisition speed by optimising the image acquisition software. Nevertheless, it is worth to be mentioned that motion artefact caused by human motion or blink may affect the imaging quality for in-vivo examination. A potential solution is to utilise line-field configuration to largely increase the imaging speed, which could be developed in the future [36]. After 3D imaging measurements, the gradient-based segmentation method was applied to extract the corneal layer interfaces. Figure 10(a) shows a resultant 3D surface plots where three distinguished interfaces including air-epithelium interface, epithelium-stroma interface, endothelium-aqueous humour interface were identified from 3D OCT data. To obtain accurate 3D segmentation results, the central corneal area (3.9×5.5 mm^2) with the best Signal-to-Noise ratio was used to perform this 3D map. In addition, Fig. 10(b) shows a 3D SI map of porcine eye with identified anterior and posterior corneal surfaces, which covers 4.0×5.8 mm^2. It was found that the air-epithelium interface of the porcine cornea can be best-fitted to an ellipsoid with a long and short radius of 7.6 mm and 6.3 mm, respectively. This agrees with the previously published results where the radius along the long and short axes was found to be 7 mm and 6 mm, respectively [33].
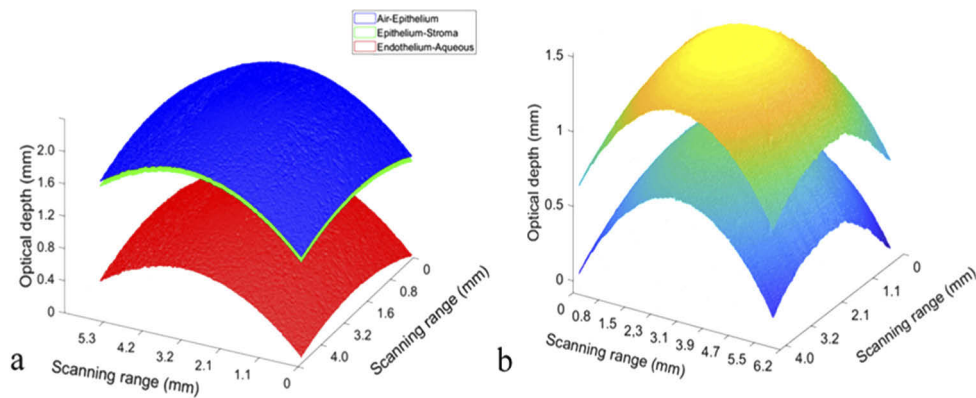

Fig. 10. 3D map of the porcine corneas. (a) Extracted corneal interfaces from OCT measurement; (b) Extracted anterior and posterior interfaces from SI measurement.

From Figs. 10(a) and 10(b), one should also be able to calculate the thickness map across the whole cornea. This is straightforward for OCT data as the corneal thickness can be easily calculated by dividing peak position difference with the refractive index. However, for SI data one has to consider the effect of refractive index on the measured corneal thickness. A mathematical correction model is needed in order to obtain the correct thickness from SI images that are acquired when the incident beam is not along the centre direction, e.g., when the incident beam is not orthogonal to the corneal apex.

4. Conclusion

In this paper, we have developed a novel combined OCT and SI device that allows both OCT and Scheimpflug images to be taken simultaneously using the same near-infrared illuminating light. The OCT images provided high axial resolution (2.7 μm in cornea), while the Scheimpflug image gave a large image depth of 12.5 mm and large field of view (16.8 $mm \times 12.5$ mm) image overview of the whole anterior chamber. Using porcine and bovine eyes *ex-vivo*, we have demonstrated that the high axial resolution OCT images resolve the details of the fine corneal-layered structure, while the Scheimpflug images gives a high-quality visualization of anterior segment. For OCT, three layers (epithelium, stroma, and the combined Descemet's and Endothelium complex) can be observed in porcine and bovine corneas. For Scheimpflug, the structure of the anterior segment

of the eye can be visualized, showing the cornea, iris, and lens. To the best of our knowledge, this is the first report that both OCT and Scheimpflug images are obtained simultaneously using the same light illumination. In addition, because both OCT and Scheimpflug images were taken simultaneously at the exact same location of a sample using the same light illumination in a single measurement, this provides a unique method for measuring both the thickness and the refractive index of each individual sample. Even though we have demonstrated ophthalmic application in this work, without a loss of generality, the proposed imaging device can also find use in other areas [37–41].

Funding

Acknowledgement

Disclosures

The authors declare no conflicts of interest.

References

1. T. Lai and S. Tang, "Cornea characterization using a combined multiphoton microscopy and optical coherence tomography system," Biomed. Opt. Express **5**(5), 1494–1511 (2014).
2. A. Foster and S. Resnikoff, "The impact of Vision 2020 on global blindness," Eye **19**(10), 1133–1135 (2005).
3. C. J. Pavlin, K. Harasiewicz, and F. S. Foster, "Ultrasound biomicroscopy of anterior segment structures in normal and glaucomatous eyes," Am. J. Ophthalmol. **113**(4), 381–389 (1992).
4. P. H. Aristides Konstantopoulos and D. F. Anderson, "Recent advances in ophthalmic anterior segment imaging: a new era for ophthalmic diagnosis?" Br. J. Ophthalmol. **91**(4), 551–557 (2007).
5. M. A. Shousha, V. L. Perez, J. Wang, T. Ide, S. Jiao, Q. Chen, V. Chang, N. Buchser, S. R. Dubovy, and W. Feuer, "Use of ultra-high-resolution optical coherence tomography to detect in vivo characteristics of Descemet's membrane in Fuchs' dystrophy," Ophthalmology **117**(6), 1220–1227 (2010).
6. R. J. Antcliff, M. R. Stanford, D. S. Chauhan, E. M. Graham, D. J. Spalton, J. S. Shilling, and J. Marshall, "Comparison between optical coherence tomography and fundus fluorescein angiography for the detection of cystoid macular edema in patients with uveitis," Ophthalmology **107**(3), 593–599 (2000).
7. B. R. Masters, "Correlation of histology and linear and nonlinear microscopy of the living human cornea," J. Biophotonics **2**(3), 127–139 (2009).
8. C. H. Sui, S. J. Wo, N. Gao, D. Y. Xu, Y. H. Han, and C. N. Du, "Design and Implementation of Digital Slit-lamp Microscope Optical System," Guangzi Xuebao **46**(7), 722001 (2017).
9. R. Jain, "Pentacam: principle and clinical applications," Current Journal of Glaucoma Practice with DVD, 20–32 (2009).
10. N. Brown, "An advanced slit-image camera," Br. J. Ophthalmol. **56**(8), 624–631 (1972).
11. J. T. Wilensky, "Relationship between corneal thickness and measured intraocular pressure in a general ophthalmology clinic - Discussion," Ophthalmology **106**(11), 2160 (1999).
12. J. M. Sparrow, N. A. P. Brown, G. A. Shunshin, and A. J. Bron, "The Oxford modular cataract image analysis system," Eye **4**(4), 638–648 (1990).
13. K. Sasaki, "The multi-purpose camera: a new anterior eye segment analysis system," Ophthalmic Res. **22**(1), 3–8 (1990).
14. T. M. Rabsilber, R. Khoramnia, and G. U. Auffarth, "Anterior chamber measurements using Pentacam rotating Scheimpflug camera," J. Cataract Refractive Surg. **32**(3), 456–459 (2006).
15. H. Shankar, D. Taranath, C. T. Santhirathelagan, and K. Pesudovs, "Anterior segment biometry with the Pentacam: Comprehensive assessment of repeatability of automated measurements," J. Cataract Refractive Surg. **34**(1), 103–113 (2008).
16. M. Dubbelman and G. L. Van der Heijde, "The shape of the aging human lens: curvature, equivalent refractive index and the lens paradox," Vision Res. **41**(14), 1867–1877 (2001).
17. D. Huang, E. A. Swanson, C. P. Lin, J. S. Schuman, W. G. Stinson, W. Chang, M. R. Hee, T. Flotte, K. Gregory, and C. A. Puliafito, "Optical coherence tomography," Science **254**(5035), 1178–1181 (1991).

18. J. A. Izatt, M. R. Hee, E. A. Swanson, C. P. Lin, D. Huang, J. S. Schuman, C. A. Puliafito, and J. G. Fujimoto, "Micrometer-scale resolution imaging of the anterior eye in-vivo with optical coherence tomography," Arch. Ophthalmol. **112**(12), 1584–1589 (1994).

19. J. L. B. Ramos, Y. Li, and D. Huang, "Clinical and research applications of anterior segment optical coherence tomography - a review," Graefes Arch. Clin. Exp. Ophthalmol. **37**(1), 81–89 (2009).

20. R. M. Werkmeister, S. Sapeta, D. Schmidl, G. Garhöfer, G. Schmidinger, V. A. dos Santos, G. C. Aschinger, I. Baumgartner, N. Pircher, and F. Schwarzhans, "Ultrahigh-resolution OCT imaging of the human cornea," Biomed. Opt. Express **8**(2), 1221–1239 (2017).

21. L. M. Vajzovic, C. L. Karp, P. Haft, M. A. Shousha, S. R. Dubovy, V. Hurmeric, S. H. Yoo, and J. Wang, "Ultra high-resolution anterior segment optical coherence tomography in the evaluation of anterior corneal dystrophies and degenerations," Ophthalmology **118**, 1291–1296 (2011).

22. M. Ang, M. Baskaran, R. M. Werkmeister, J. Chua, D. Schmidl, V. A. Dos Santos, G. Garhöfer, J. S. Mehta, and L. Schmetterer, "Anterior segment optical coherence tomography," Prog. Retinal Eye Res. **66**, 132–156 (2018).

23. Q. Yang, C. A. Reisman, Z. Wang, Y. Fukuma, M. Hangai, N. Yoshimura, A. Tomidokoro, M. Araie, A. S. Raza, and D. C. Hood, "Automated layer segmentation of macular OCT images using dual-scale gradient information," Opt. Express **18**(20), 21293–21307 (2010).

24. M. G. Wirtitsch, O. Findl, H. Heinzl, and W. Drexler, "Effect of dorzolamide hydrochloride on central corneal thickness in humans with cornea guttata," Arch. Ophthalmol. **125**(10), 1345–1350 (2007).

25. M. G. Wirtitsch, O. Findl, B. Kiss, V. Petternel, H. Heinzl, and W. Drexler, "Short-term effect of dorzolamide hydrochloride on central corneal thickness in humans with cornea guttata," Arch. Ophthalmol. **121**(5), 621–625 (2003).

26. S. Bak-Nielsen, I. B. Pedersen, A. Ivarsen, and J. Hjortdal, "Dynamic Scheimpflug-based assessment of keratoconus and the effects of corneal cross-linking," J. Refract. Surg. **30**(6), 408–414 (2014).

27. S. Shah, M. Laiquzzaman, R. Bhojwani, S. Mantry, and I. Cunliffe, "Assessment of the biomechanical properties of the cornea with the ocular response analyzer in normal and keratoconic eyes," Invest. Ophthalmol. Visual Sci. **48**(7), 3026–3031 (2007).

28. L. W. Herndon, J. S. Weizer, and S. S. Stinnett, "Central corneal thickness as a risk factor for advanced glaucoma damage," Arch. Ophthalmol. **122**(1), 17–21 (2004).

29. T. Li, L. Tian, L. Wang, Y. Hon, A. K. Lam, Y. Huang, Y. Wang, and Y. Zheng, "Correction on the distortion of Scheimpflug imaging for dynamic central corneal thickness," J. Biomed. Opt. **20**(5), 056006 (2015).

30. 1. J. Fournier and E. Snitzer, "The nonlinear refractive index of glass," IEEE J. Quantum Electron. **10**(5), 473–475 (1974).

31. S. R. Uhlhorn, F. Manns, H. Tahi, P. O. Rol, and J.-M. A. Parel, "Corneal group refractive index measurement using low-coherence interferometry," in *Ophthalmic Technologies VIII*, (International Society for Optics and Photonics, 1998), 14–21.

32. Y. L. Kim, J. T. Walsh, T. K. Goldstick, and M. R. Glucksberg, "Variation of corneal refractive index with hydration," Phys. Med. Biol. **49**(5), 859–868 (2004).

33. I. Sanchez, R. Martin, F. Ussa, and I. Fernandez-Bueno, "The parameters of the porcine eyeball," Graefe's Arch. Clin. Exp. Ophthalmol. **249**(4), 475–482 (2011).

34. C. Faber, E. Scherfig, J. U. Prause, and K. E. Sørensen, "Corneal thickness in pigs measured by ultrasound pachymetry in vivo," Scand J Lab Anim Sci **35**, 39–43 (2008).

35. J. Heichel, F. Wilhelm, K. S. Kunert, and T. Hammer, "Topographic findings of the porcine cornea," Medical Hypothesis, Discovery and Innovation in Ophthalmology **5**, 125 (2016).

36. S. Lawman, Y. Dong, B. M. Williams, V. Romano, S. Kaye, S. P. Harding, C. Willoughby, Y. C. Shen, and Y. L. Zheng, "High resolution corneal and single pulse imaging with line field spectral domain optical coherence tomography," Opt. Express **24**(11), 12395–12405 (2016).

37. D. Stifter, "Beyond biomedicine: a review of alternative applications and developments for optical coherence tomography," Appl. Phys. B **88**(3), 337–357 (2007).

38. J. M. Schmitt, "Optical coherence tomography (OCT): a review," IEEE J. Sel. Top. Quantum Electron. **5**(4), 1205–1215 (1999).

39. H. Lin, Z. Zhang, D. Markl, J. A. Zeitler, and Y. Shen, "A review of the applications of OCT for analysing pharmaceutical film coatings," Appl. Sci. **8**(12), 2700 (2018).

40. Z. Zhang, U. Ikpatt, S. Lawman, B. Williams, Y. Zheng, H. Lin, and Y. Shen, "Sub-surface imaging of soiled cotton fabric using full-field optical coherence tomography," Opt. Express **27**(10), 13951–13964 (2019).

41. H. Lin, Y. Dong, D. Markl, Z. Zhang, Y. Shen, and J. A. Zeitler, "Pharmaceutical film coating catalog for spectral domain optical coherence tomography," J. Pharm. Sci. **106**(10), 3171–3176 (2017).